Veloso, AD, Ferraria, AM, Botelho do Rego, AM, Viana, AS, Fernandes, AJS, Fielding, AJ, Videira, RA and Oliveira, MC

Structural effects induced by dialysis-based purification of carbon nanomaterials

Nano Materials Science 6 (2024) 475–483

Contents lists available at ScienceDirect

Nano Materials Science

journal homepage: www.keaipublishing.com/cn/journals/nano-materials-science/

Structural effects induced by dialysis-based purification of carbon nanomaterials

A.D. Veloso [a], A.M. Ferraria [b], A.M. Botelho do Rego [b], A.S. Viana [c], A.J.S. Fernandes [d], A.J. Fielding [e], R.A. Videira [f], M.C. Oliveira [a,*]

[a] CQ-VR and Chemistry Department, University of Trás-os-Montes e Alto Douro, 5000-801, Vila Real, Portugal
[b] BSIRG, iBB - Institute for Bioengineering and Biosciences, Department of Chemical Engineering, and Associate Laboratory i4HB - Institute for Health and Bioeconomy, Instituto Superior Técnico, Universidade de Lisboa, 1049-001, Lisbon, Portugal
[c] Centro de Química Estrutural, Institute of Molecular Sciences, Departamento de Química e Bioquímica, Faculdade de Ciências, Universidade de Lisboa, Campo Grande, 1749-016, Lisboa, Portugal
[d] I3N and Physics Department, University of Aveiro, Campus de Santiago, 3810-193, Aveiro, Portugal
[e] Faculty of Science, Pharmacy and Biomolecular School, Liverpool John Moores University, United Kingdom
[f] REQUIMTE/LAQV, Laboratório de Farmacognosia, Departamento de Química, Faculdade de Farmácia, Universidade do Porto, 4050-313, Porto, Portugal

ARTICLE INFO

Keywords:
Nanocarbon
Surface functionalization
NMR
XPS
Hydrophilic carbon
Paramagnetic

ABSTRACT

Dialysis plays a crucial role in the purification of nanomaterials but its impact on the structural properties of carbon nanomaterials was never investigated. Herein, a carbon-based nanomaterial generated electrochemically in potassium phosphate buffer, was characterized before and after dialysis against pure water. It is shown that dialysis affects the size of the carbon domains, structural organization, surface functionalization, oxidation degree of carbon, and grade of amorphicity. Accordingly, dialysis drives the nanomaterial organization from discrete roundish carbon domains, with sizes ranging from 70 to 160 nm, towards linear stacking structures of small nanoparticles (<15 nm). In parallel, alcohol and ether (epoxide) surface groups evolve into more oxidized carbon groups (e.g., ketone and ester groups). Investigation of the as-prepared nanomaterial by electron paramagnetic resonance (EPR) revealed a resonance signal consistent with carbon-oxygen centred radicals.

Additionally, this study brings to light the selective affinity of the carbon nanomaterial under study to capture Na^+ ions, a property greatly enhanced by the dialysis process, and its high ability to trap oxygen, particularly before dialysis. These findings open new perspectives for the application of carbon-based nanomaterials and raise awareness of the importance of structural changes that can occur during the purification of carbon-based nanomaterials.

1. Introduction

The importance of knowing the structure-property relationship is a common denominator in the field of chemistry and materials sciences, and the key for the development of new molecules and materials in response to new societal demands. However, the study of the structure-property dualism presents multiple challenges. In the field of carbon nanoparticles, the demands are placed both in terms of producing nanoparticles with a uniform range of sizes and structures, as well as on ensuring a reliable structural characterization [1].

Ambiguities may arise if the acquired characterization data is not representative of the whole sample, or if the characterization techniques are not able to distinguish the core from the surface of the carbon nanoparticle [2]. Furthermore, results may be biased by potential structural modifications induced by the incident radiation used in a given technique of analysis, like electron or laser beams. This last situation is relevant for amorphous carbon nanomaterials where it was reported that the incidence of high-power beams may promote the formation of crystalline phases [3,4], such as in Raman or in Transmission Electron Microscopy techniques.

Another matter of fundamental relevance, rarely discussed in the literature, is related to the fact that carbon nanomaterial structures are usually characterized in a medium free-of-electrolyte, in other words, in a chemical environment very different from the one where their properties are exhibited. The electrolyte removal is a consequence of the physical processes needed for the separation and isolation of the carbon-based

* Corresponding author.
E-mail address: mcris@utad.pt (M.C. Oliveira).

https://doi.org/10.1016/j.nanoms.2023.12.002
Received 23 August 2023; Accepted 6 December 2023
Available online 16 December 2023

nanomaterial after its synthesis. The most common procedures for this purpose are chromatography, filtration, centrifugation, and dialysis. However, the extent to which the removal of the electrolyte induces chemical and structural alterations in carbon nanomaterials remains completely unknown, and the assumption that the structure of the as-prepared carbon-based nanomaterial does not suffer any modification along the separation and isolation steps is broadly taken for granted.

When nanomaterials are synthesized via electrochemical approaches, this issue is even more important. This is because the electrolyte, which is used to minimize solution resistivity, may remain together with the carbon-based nanomaterial in a wide range of applications, not demanding the separation of the carbon nanomaterial from the electrolytic medium. The non-separation of the electrolyte is very attractive because it simplifies the entire manufacturing process, increasing its efficiency, and reducing the time and resources needed. However, this issue calls for structural-properties studies based on the characterization of the nanomaterial as it is obtained after synthesis, without separating it from the electrolyte.

It was framed by this concern that the present work was undertaken. The object of this study was a water-soluble carbon nanomaterial released electrochemically from an anode of graphite after 1 h under strong polarization (0.06 A) in a two-compartment cell. The short synthesis time was intentional to avoid a large dispersion of nanoparticle sizes and structures [5]. Accordingly, at the end of the galvanostatic assay the anolyte is clear and transparent, with no traces of graphitic chunks in the solution. As it will be explained below, the carbon-based nanomaterial electrogenerated in such experimental conditions has been the subject of several studies in our group [5–8] but, so far, the properties of this material have been solely explored as a conductive electrode material, implying its separation from the electrolyte. In fact, the mainstream approach for the structural characterization of carbon-based nanomaterials primarily focuses on the carbon-based solution after the dialysis process [9,10].

The electrochemical synthesis of carbon nanomaterials by a top-down approach is widely used in the production of 0-D nanoparticles [11,12]. Yet, the carbon-based material generated under our experimental set-up shows, after the removal of the electrolyte, a dual behaviour that differentiates it from other 0-D carbon nanomaterials, behaving either as an electrolyte in aqueous medium or a conductive material in the solid state [6]. In terms of size, these nanomaterials resemble carbon dots, but various other features make them unique, including a high oxygen/-carbon ratio, outstanding solubility in water, and no solubility in organic solvents. Thus, to distinguish them from carbon dots, they have been called Electrogenerated Hydrophilic Carbon nanomaterials (EHC).

Hence, the main objective of this work is to investigate the impact of the dialysis process on the structure of the EHC material. For this purpose, a systematic characterization of the EHC nanomaterial was undertaken, both in the presence and absence of the electrolyte where it was generated (phosphate buffer). For the sake of clarification, as-generated EHC is represented by the acronym EHC_{prep} and post-dialysis EHC is labelled as $EHC_{dial.}$

2. Experimental

2.1. Synthesis of EHC

The electrochemical synthesis of the EHC material was described elsewhere [7]. Shortly, the synthesis was performed in a three-compartment cell containing a 0.05 M K_2HPO_4 + 0.05 M KH_2PO_4 solution (chemicals supplied from Merck; Suprapur grade, 99.99 %) at pH 6.8. Graphite rods from Goodfellow (99.997 %) were used as anode (working electrode) and cathode (counter electrode), and a saturated calomel electrode (SCE) was used as reference electrode. The solution was thoroughly deoxygenated in the cell with argon and an inert atmosphere was maintained during the synthesis. The polarization was performed under galvanostatic mode (I = 0.06 A), for 1 h, using an Autolab PGSTAT100 potentiostat/galvanostat controlled by GPES software. To generate independent samples, successive synthesis assays were performed (n > 6). To mitigate the rapid degradation of the anode material and maintain approximately the anode surface conditions throughout the various syntheses, the same graphite rod was employed alternately as both anode and cathode. Additionally, a pre-treatment procedure was executed prior to each synthesis to eliminate oxidized and weakly adherent particles from the cathode electrode. For this purpose, a 60 mA current was applied for 400 s in the phosphate buffer solution. Typically, this process results in a brownish solution in the cathodic compartment, which is replaced with a fresh buffer solution before initiating the synthesis assay. After the galvanostatic polarization, the solution from the anodic compartment was removed and stored at 4 °C, giving rise to the so-called EHC_{prep} solution. Alternatively, this solution was subject to dialysis using a 3.5–5 kDa molecular weight cut-off membrane and ultrapure water ($V_{sample} \cong$ 7 mL and $V_{H2O} \cong$ 500 mL). Unless otherwise stated, dialysis was performed for approximately 48 h, giving birth to the EHC_{dial} solution. During the first 6 h of dialysis, the conductivity of the water outside the membrane was monitored and the water was replaced every time the osmotic equilibrium was attained to enable the continuous output of the electrolyte ions. After this period, the water was replaced every 5 h. The EHC_{dial} solutions that were characterized by ATR-FTIR were further subjected to evaporation at 50 °C and then dissolved in ultrapure water to concentrate the EHC material. This analysis relies on the assumption that the structure of the nanomaterial is preserved along the evaporation stage.

The carbon content in EHC_{prep} and $EHC_{dial.}$ solutions were 17.6 ± 2.6 mg C/L (n = 5) and 6.7 ± 1.4 mg C/L (n = 5), respectively, and the corresponding pH was 2.7 and 5.1.

2.2. Characterization

Atomic Force Microscopy (AFM) measurements were conducted using a Nanoscope IIIa Multimode instrument produced by Digital Instruments (Veeco, Santa Barbara, CA) in tapping mode, with etched silicon tips with a resonance frequency of ca. 300 kHz, at a scan rate of ca. 1.5 Hz, in ambient conditions (~21 °C). For each measurement, approximately 10 μl of each EHC solution was dropped onto a freshly cleaved mica and kept in contact for 15 min. They were then rinsed with water and dried with a nitrogen gas flow. For better clarification of the structural organization of EHC_{dial}, this sample was also prepared on a HOPG substrate. Operation conditions and image acquisition are described elsewhere [7]. Typically, for each sample, approximately 3–4 different areas were examined.

Attenuated Total Reflectance Fourier-Transform Infrared (ATR-FTIR) spectroscopy was carried out at room temperature on a spectrometer (IRAffinity-1S, Shimadzu) coupled to a Quest^{TM} ATR accessory containing a diamond crystal (Specac), using 128 scans at a resolution of 2 cm^{-1} in a 4000 to 400 cm^{-1} range. For comparison purposes, the electrolyte spectrum was also recorded. The samples were prepared after successive depositions of 5 μL, followed by air drying until a final volume of 20 μL was reached. To ensure that the samples were completely dry, the spectra were recorded successively during the evaporation period until the contribution of water bands was no longer observed.

Transmission Electron Microscopy (TEM) images were acquired with a 100 kV Jeol JEM-1010 microscope equipped with a CCD Orius camera and a Digital Montage Plug-in. The samples were prepared by immersing a copper grid in the EHC solution.

Analysis of AFM on mica, FTIR-ATR, and TEM were conducted using a minimum of three independent samples of both EHC_{prep} and EHC_{dial}. The results shown in this manuscript are representative of the obtained data.

The ^{1}H and ^{31}P Nuclear Magnetic Resonance (NMR) spectra were recorded in D_2O at 298 K on a Bruker ARX 400 spectrometer (at 400 and 162 MHz, respectively). ^{1}H NMR spectra were recorded with two independent samples, while the ^{31}P NMR spectrum was obtained from a single synthesized sample.

X-ray Photoelectron Spectroscopy (XPS) characterization was performed with a dual-anode XSAM800 spectrometer from KRATOS. XPS samples of EHC_{prep} and EHC_{dial} were prepared by successive steps of drop/evaporation of the solutions ($V_{total} \cong$ 500 μL) on Si solid substrates with no particular etching procedure. Multiple depositions were done until the substrate was completely covered by a noticeably thick EHC organic layer. Samples were dried at room temperature under vacuum at 0.1 bar. Mg Kα and Al Kα X-radiation were used. Operational conditions and data treatment details were as published elsewhere [5].

Electron paramagnetic resonance (EPR) spectra were recorded at 120 K using a Bruker EMX microspectrometer. The EHC_{prep} solution was frozen in a 4-mm EPR tube using liquid nitrogen. The microwave frequency was 9.4296 GHz, microwave power 0.06325 mW, and the modulation amplitude 2.0 G. The analysis was performed in duplicate with two aliquots of the same sample. A control solution (buffer electrolyte) was also used under the same conditions. No EPR signal was obtained.

The Raman spectra were acquired by an open-air Jobin Yvon HR800 micro-Raman spectrometer (Horiba Group, Japan) using the native laser source of the Raman instrument (633 nm red line) with a 100× Olympus objective (NA = 0.9). For this analysis, 5 μL of the EHC solutions were deposited onto a quartz slide and allowed to dry. This process was repeated four times, totaling a volume of 20 μL. The typical parameters used for the acquisitions were 5 s integration time with 2 accumulations while the laser power was set to <30 mW at the laser exit (<7 mW at the sample). The criterion to define the used power relied on obtaining successive spectra acquisitions without noticeable changes, along with microscope inspection at the laser-hitting spot. This approach was used for increasing powers from 5 mW up to 30 mW. The final value for each sample was defined as the last power level at which the spectra remained unchanged. The analyses were conducted on two independent samples of EHC_{prep} and EHC_{dial}. For each sample, approximately 3–4 different areas were examined. It was observed that the samples exhibited a high degree of uniformity.

Dynamic Light Scattering (DLS) analysis was performed using a Litesizer DLS 500 (Anton Paar GmbH) equipped with a single frequency laser diode (658 nm) at the scattering angle of 175 °C (Backscatter). Before the analysis, both samples were filtered through a 0.02 μm (Whatmant™ Anotop™) filter. The individual run time was 10 s, and at least six runs per sample were performed. A total of seven analyses were conducted on both samples.

Despite the experimental precautions to ensure the reproducibility of the electrode surface state, we are aware that synthesis after synthesis may lead to changes in the state of the surface. To check this, we employed cyclic voltammetry [13]. The results demonstrated a qualitative consistency in the electrode surface state, but not a quantitative one. For a reliable comparison between EHC_{prep} and EHC_{dial}, most of the data was obtained from the same synthesis.

3. Results

3.1. Size and morphology

Size, shape, and organization of the carbon domains in EHC_{prep} and EHC_{dial} were assessed by TEM and AFM. TEM images of EHC_{prep} material reveal a compact carbonaceous layer on which some roundish carbon dots (≅ 2 nm size) and carbon flakes are attached, Fig. 1a and b. In contrast, EHC_{dial} shows a 2D organization in which the carbon dots are no longer detected, the compactness of the carbonaceous layer is broken, and large carbon flakes and chain-like domains emerge, Fig. 1c and d.

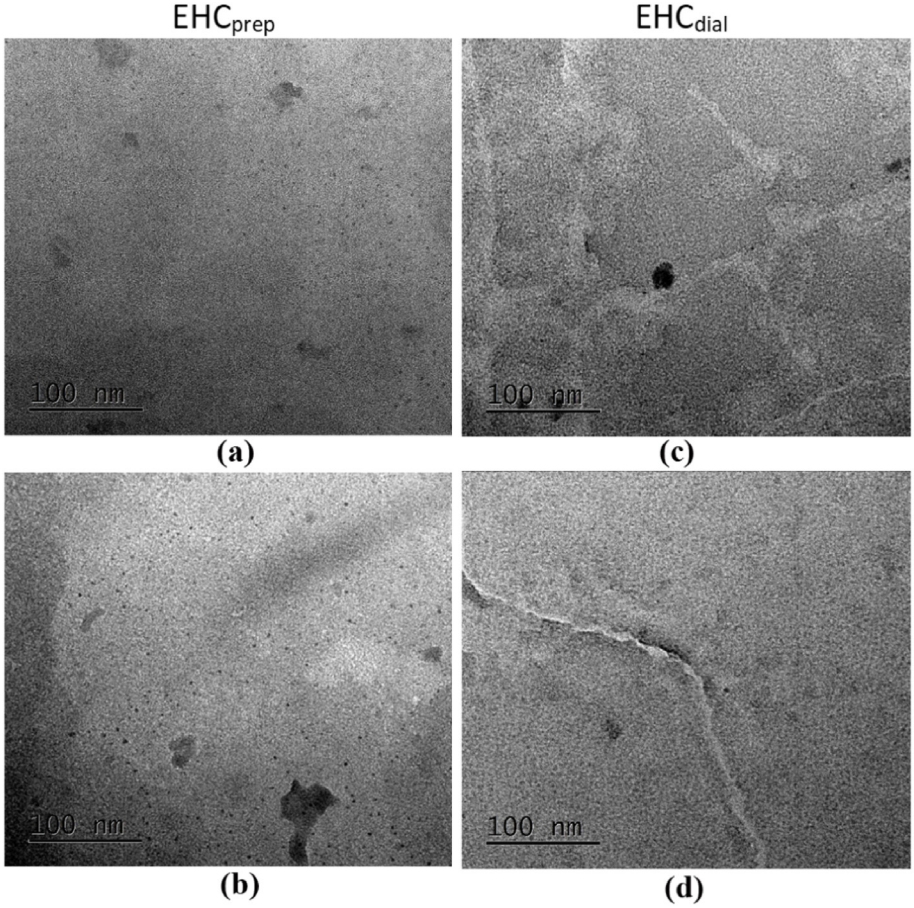

Fig. 1. TEM images of EHC_{prep} (a,b) and EHC_{dial} (c,d).

The dimensions of the building blocks of these assemblies are not discernible by TEM, probably because they are below the resolution of the equipment These materials are particularly sensitive to the electron beam, degrading quickly as they are exposed to higher-voltage beams.

These results are consistent with the data obtained by dynamic light scattering (DLS). EHC_{prep} and EHC_{dial} were found to be dominated by carbon-based populations with sizes of 1134 ± 471 nm and 832 ± 155 nm, respectively, even though filtration with a 20 nm pore-size Whatman Anatop filter was performed. These results confirm that very strong interaction forces occur between EHC units (or EHC and electrolyte ions), resulting in the formation of large assemblies.

While TEM images are acquired in an ultra-high vacuum environment, from which hydration water molecules are excluded, AFM provides three-dimensional imaging within a non-evacuated system, where water molecules are probably H-bonded to the nanoparticles. The presence of water molecules within EHC units is likely the reason why discrete nanoparticles are detected by AFM but not by TEM. Accordingly, an agglomeration of large roundish discrete nanoparticles adsorbed on mica is observed by AFM (mean thickness of 9.4 nm and a diameter of 70–160 nm), Fig. 2a. Contrary to expectations, upon the removal of the electrolyte, a mesh-like structure formed by the self-assembly of much smaller units than those detected before dialysis, appears (thickness <1 nm, diameter <15 nm), Fig. 2b. This effect is more evident when EHC_{dial} is deposited onto an HOPG substrate, revealing branches-like structures of linear stacking particles in a bi-dimensional layer, Fig. 2c.

These results suggest that the size of EHC_{prep} particles does not accurately reflect the dimensions of the individual structures released from the graphite electrode during the synthesis.

The compact layer detected by TEM and the large and discrete agglomerates detected by AFM in EHC_{prep} are probably a homogeneous mixture of the carbon-based material and electrolyte, which result from strong intermolecular forces established by the two components. Upon the removal of the electrolyte, these aggregates disassemble, leaving smaller carbon domains free for self-assembling into different 2D organizations, as shown by TEM and AFM in EHC_{dial}. Their ability to form these assemblies indicates the presence of strong intermolecular forces among EHC units in the electrolyte-free medium. Thus, despite the probable low size of the building blocks of EHC_{dial}, they are not lost through the membrane due to their capacity to interact with each other.

3.2. Composition and functionalities

X-ray photoelectron spectroscopy (XPS) allowed the comparison between EHC_{prep} and EHC_{dial} regarding atomic composition and type of carbon oxidized groups. Fig. 3 and Table 1 show, respectively, the survey XPS spectra and the atomic concentrations of the detected elements.

The most striking finding of these results is the content of sodium in as-prepared material (EHC_{prep}) since no chemicals containing sodium ions were used in the buffer phosphate (prepared with K_2HPO_4 and KH_2PO_4 salts, 99,99 %). In contrast, a relatively low amount of potassium was detected. The K^+ migration to the cathodic compartment along the electrochemical synthesis is expected to counterbalance the formation of hydronium cations at the anode. The detection of sodium has been

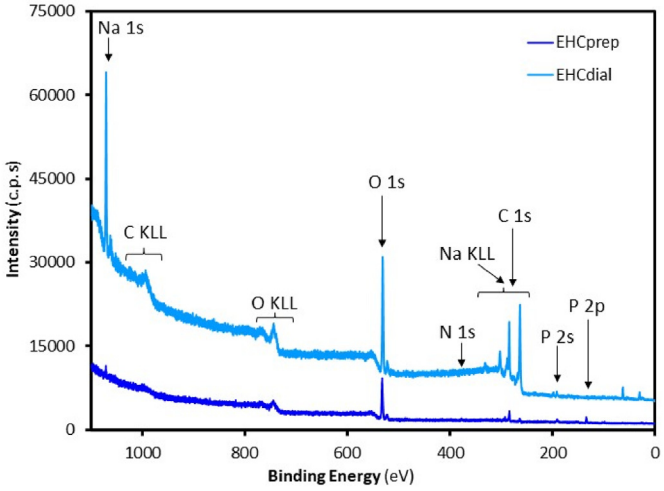

Fig. 3. Wide scan of XPS spectra of EHC_{prep} and EHC_{dial}.

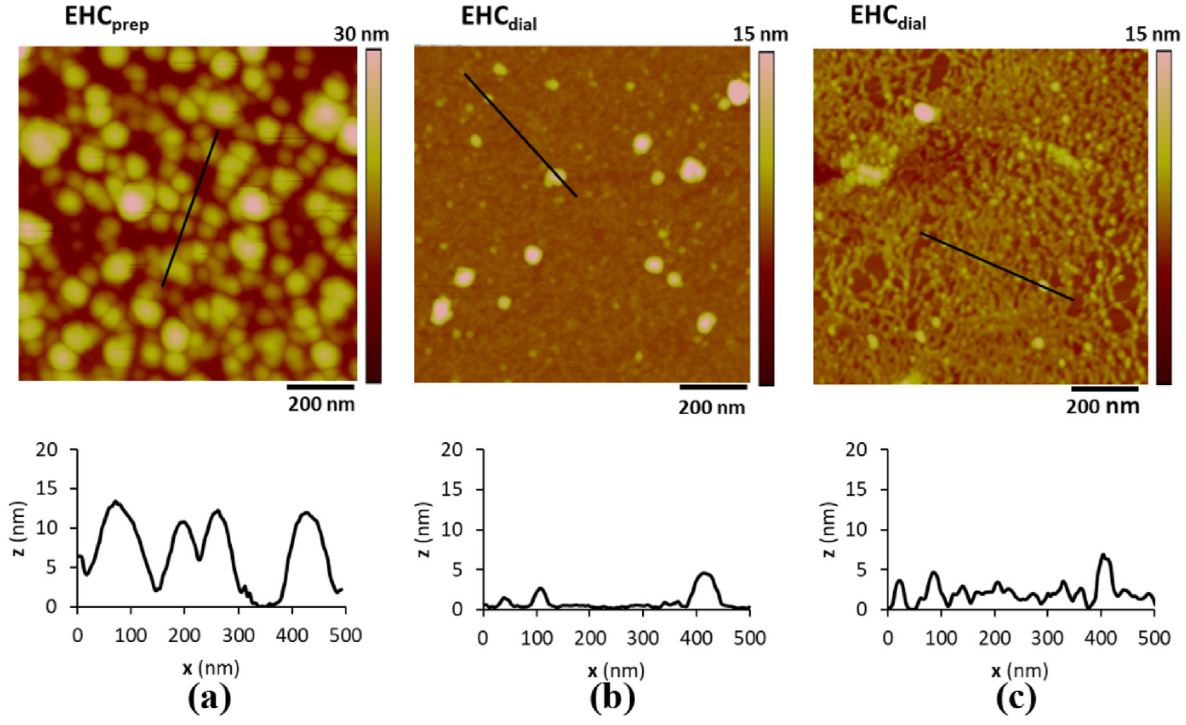

Fig. 2. AFM images of EHC_{prep} deposited on mica (a) EHC_{dial} deposited on mica (b) and on HOPG (c); corresponding height profiles.

Table 1
Atomic composition of EHC_{prep} and EHC_{dial} obtained from XPS and atomic ratios Na/C and Na/O.

Element	Atomic concentration (at. %)	
	EHC_{prep}	EHC_{dial}
C	30.5	39.3
O	54.1	35.3
Na	4.7	23.4
K	2.0	n.d.
P	7.4	0.5
N	1.2	0.7
Cl	n.d.	0.7
Atomic ratio		
Na/C	0.15	0.59
Na/O	0.09	0.66

repeatedly found in independent samples prepared in slightly different conditions. Accordingly, sodium has been found when the synthesis was performed in the same buffer but exposed to air [6] or N_2 gas [7], or when different galvanostatic conditions were applied [5], or when other electrolytes were used as buffers (citrate and glycine) [14,15], and even when EHC was released in the cathodic compartment in phosphate buffer [7]. It is very likely that this phenomenon may have been observed by other researchers but was never reported before.

The detection of sodium in detriment of potassium is indicative of an extraordinary affinity of the carbonaceous nanomaterial for sodium, which is even greater after the electrolyte removal by the dialysis process, as attested by the huge atomic concentration computed from EHC_{dial} XPS data (Table 1). Two key questions may be raised from these findings: What is the source of sodium in the solution? How are the sodium ions charge-balanced?

To check whether the dialysis membrane is responsible for the sodium source, both faces of the membranes were analysed by XPS, but no sodium was detected on the dialysis membrane, Fig. 4. Apart from the dialysis membrane, the carbon-based solution is also in contact with the glass material (electrochemical cell and solution storage vials). To evaluate whether the glass material could be the source of sodium, the EHC_{prep} solution (inevitably prepared in a glass cell) was stored for one month in either a plastic container or in a glass vial, and both were analysed by XPS. It was detected 4.7 at. % of sodium in the sample stored in the plastic container and 23.4 at. % in the sample stored in the glass. Comparison of the wide spectra is shown in Fig. 4. These results confirm the hypothesis that sodium ion originates from the contact of the EHC solution with glass material. Despite this, there are still multiple questions that remain unanswered, including how sodium ions are leached out from the glass by the EHC material and what makes this material so selective to sodium ions. The observation that EHC exhibits a high affinity for Na^+ has no parallel in carbon-based nanomaterials. These findings open new perspectives for the application of carbon-based nanomaterials, such as in biomedicine, energy storage, and sensing.

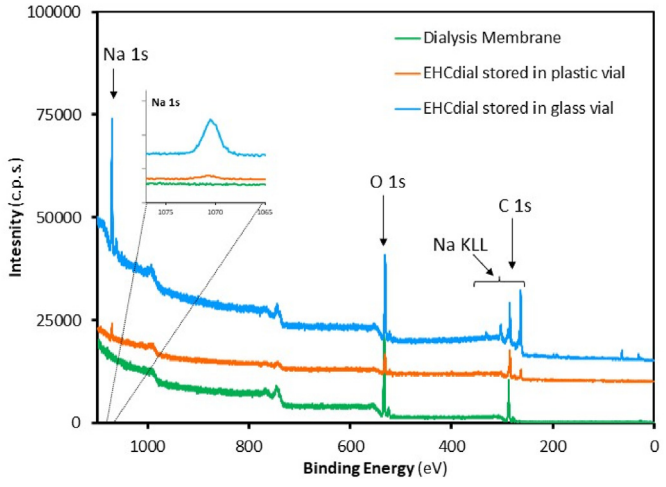

Fig. 4. Wide scan of XPS spectra of the dialysis membrane, and EHC_{dial} solutions stored in a plastic vial or in a glass vial. The inset shows the Na 1s region.

Compared to EHC_{prep}, the highest affinity of EHC_{dial} to capture Na^+ is well reflected in the ratios of Na/O and Na/C of these materials: respectively 0.66 and 0.59 in EHC_{dial} against 0.09 and 0.15 in EHC_{prep}. This finding reinforces the conclusion that the electrolyte removal from the EHC solution promotes a new molecular architecture, and consequently, the emergence of novel properties.

Besides sodium, chloride and nitrogen are also detected, but in much smaller amounts. Chloride comes from the reference electrode (SCE) while nitrogen has been demonstrated to be originated from the N_2 gas present in the aqueous medium [7]. The detection of nitrogen-carbon bonds provides a hint regarding the formation of very strong reactive species, probably radical species. This hypothesis is supported by the EPR results, as it will be demonstrated below.

XPS also provides valuable insights into the chemical states of carbon atoms. EHC_{prep} and EHC_{dial} C 1s regions were fitted simultaneously with six peaks in the same positions, as described previously [5]. The obtained spectra are shown in Fig. 5a. Binding energies (BE), atomic concentrations, and assignments are included in Table 2. Besides C–C and/or C–H sp^3 and sp^2 carbon atoms, C–N and C–O single bonds and carbon atoms with very electronegative vicinities, like in carboxylate and carboxylic can exist before and after dialysis. EHC_{dial} also shows the presence of carbonyl (C═O) or acetal (O–C–O) functions that seem to be absent in EHC_{prep}. In detail, the C 1s region of EHC_{prep} shows that the peak at 287 eV is the most important oxygen group detected. This peak has the contribution of epoxides and carbon bonded to oxygen, like in ether (C–O–C) or alcohol (C–OH) groups. In addition, it is also detected a peak at 286.2 eV in EHC_{prep} attributed to carbon singly bonded to nitrogen. The peak centred at 289 eV is assigned to carbon from an ester ((C═O)–O–C), carboxylic (-COOH), or carboxylate (COO^-) groups. In contrast, the most important peak of EHC_{dial} is centred at slightly higher binding energy, 288 eV, corresponding to carbonyl (C═O), O–C–O or carbon in amide ((CO)–NH-) groups. The large chemical shift suggests that epoxides and C–O single bond groups on EHC_{prep} evolve to a more oxidized form of carbon, like carbonyl, O–C–O, or amide groups upon the dialysis process. Accordingly, it is also shown that dialysis is accompanied by a higher degree of carbon oxidation as computed by the atomic ratio C_{ox}/C in EHC_{prep} and EHC_{dial}, 0.19 and 0.32, respectively (C_{ox} is the relative amount of carbon covalently bonded to oxygen, as described in Table 2). This conclusion is also supported by O 1s spectra (Fig. 5b).

The carbon functional groups summarized in Table 2 were identified bearing in mind that probable superpositions may occur, since some of these features can be found roughly within a BE window of 2 eV,

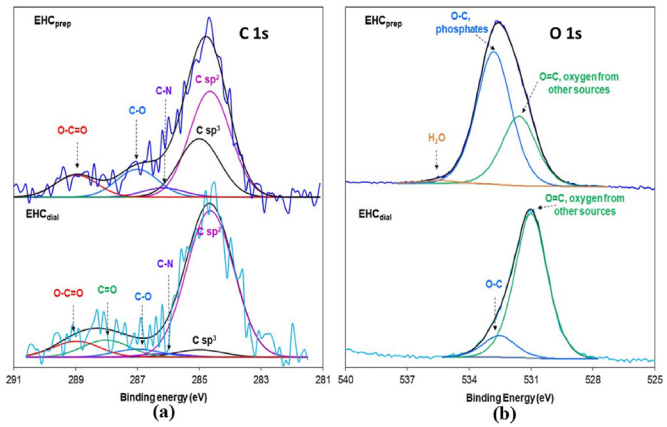

Fig. 5. XPS C 1s (a) and O 1s (b) regions of EHC_{prep} and EHC_{dial}.

Table 2
Binding energies (BE, eV), corresponding assignments, atomic concentrations (%) [in brackets], and atomic ratios computed from XPS spectra of EHC_{prep} and EHC_{dial}. It is included the charge balance of each system.

Region	EHC_{prep}	EHC_{dial}	Assignments	q_i
C 1s	284.7 [14.4]	284.7 [28.9]	C–C and/or C–H sp^2	
	285.0 [8.0]	285.0 [1.5]	C–C and/or C–H sp^3	
	286.2 [1.3]	286.2 [0.8]	C–N	
	287.0 [3.8]	287.0 [1.6]	-C-O- and/or epoxide	
	–	288.0 [3.4]	C═O or O–C–O, –C═O–NH	
	289.0 [3.1]	289.0 [3.2]	O–C═O^-, COOH, π-π[a]	−1
K $2p_{3/2}$	293.2 [1.3]	–	K^+	+1
K $2p_{1/2}$	296.0 [0.7]	–		
O 1s	531.6 [20.2]	531.0 [31.5]	O═C, oxygen from other sources	
	532.8 [33.1]	532.5 [3.8]	O–C, phosphates	
	535.5 [0.8]	–	H_2O	
P $2p_{3/2}$	134.1 [5.0]	132.9 [0.3]	PO_4^{3-} or HPO_4^{2-} or $H_2PO_4^-$	−3[a], −2, or −1
P $2p_{1/2}$	135.0 [2.5]	133.8 [0.2]		
N 1s	400.1 [0.5]	399.7 [0.7]	NH_2	
	401.9 [0.7]	–	N^+	+1
Na 1s	1071.3 [4.7]	1070.7 [23.4]	Na^+	+1
Cl $2p_{3/2}$	–	198.3 [0.5]	Cl^-	−1
Cl $2p_{1/2}$	–	200.0 [0.2]		
C_{ox}/O	0.19	0.32		
(O-O_{ox})/Na	2.91	0.94		
Σ_i([at. %]$_i$ × q_i)	−3.0	18.0		

[a] Used to calculate the overall charge.

depending on the atomic vicinity (whose composition can also vary considerably). Some uncertainty may also arise from a particular data treatment performed in this case: before any peak fitting, the Na KLL Auger structure, detected in the same energy window as C 1s when using the Mg Kα X-ray source, had to be subtracted from the C 1s spectra to avoid misleading assignments. The subtraction of the Na Auger features was possible after obtaining the Na KLL region free of any superpositions using the Al Kα X-ray source. Despite these difficulties, a more reliable chemical characterization of these EHC nanomaterials can be reached when corroborated by a quantitative analysis.

In Table 2, the overall charge of each solution was computed from the product of the atomic % by the oxidation state of each ionic species. The excess of positive charge in the system has been raised before [6]. To explain this phenomenon, it has been proposed that the positive charge may arise from long-range dipolar effects and may be neutralized by negative charges in the π delocalized system. Herein we reappraise this subject by analysing another possible provenance of the negative charge that is required to balance the excess of the positive charge: the oxygen not covalently bonded to carbon. Accordingly, the atomic ratio (O-O_{ox})/Na was computed, where O-O_{ox} represents the amount of oxygen not covalently bonded to carbon, phosphorous, or in water. In this calculation, "O" is the total relative amount of oxygen, and "O_{ox}" = 4 × P + (C single bond to O) + (C double bond to O) + 2 × (C in COO^-) + H_2O, where the different carbon species were computed from the peaks fitted in C 1s (Table 2 and Fig. 5). Data shown in Table 2 reveals that the ratio (O-O_{ox})/Na is close to 3 in EHC_{prep}, and close to 1 in EHC_{dial}. For EHC_{dial}, the (O:Na) 1:1 ratio is consistent with the presence of sodium peroxide (Na_2O_2) or monohydrated sodium oxide ($Na_2O.H_2O$). In the case of EHC_{prep}, the (O-O_{ox})/Na ratio is unexpectedly high. The (O:Na) 3:1 ratio cannot be explained by any sodium oxide unless an excess of oxygen is also considered. This excess of oxygen could be rationalized in two ways: first, considering that H_2O_2 is co-generated during EHC formation, and second, by accepting that some of the co-generated O_2 is strongly trapped in the host carbonaceous material. The EHC_{prep} solution was analysed by Raman spectroscopy (data shown below) and tested using peroxide test strips (Quantofix from Macherey-Nagel; detectable range: 5–25 mg/L), but no H_2O_2 was detected. Therefore, we conclude that the EHC_{prep} material can effectively trap oxygen molecules. The strong interaction between carbon nanomaterials and molecular oxygen is well-known, particularly in fullerene-derived and nanotubes nanomaterials [16,17].

The finding that the carbon-based nanomaterial is combined with sodium oxide species allows us to understand some previously reported properties of EHC_{dial}, such as its unexpected insolubility in organic solvents and electrolyte-like behaviour [6].

Further characterization of the functional groups in EHC nanomaterial was performed by ATR-FTIR spectroscopy. Information from the EHC_{prep} spectrum was difficult to extract due to the dominance of P–O and P═O IR bands over the 1300-600 cm^{-1} wavenumber range. To minimize this issue the IR spectrum was taken at two different points of the dialysis process, after 6 and 48 h, labelled respectively as short-term and long-term dialysis. The spectra of short-termed and long-termed EHC_{dial} are shown in Fig. 6.

For a better comparison, it is also included the spectrum of the phosphate buffer. Short-termed EHC_{dial} shows characteristic bands of P–O at 941 cm^{-1} indicative that phosphate electrolyte remains in the solution. Despite ν_s (P–O) and ν_{as} (P–O–C) modes absorbing in the same wavenumber range, the possibility of C–O–P bond formation was dismissed based on the ^{31}P RMN spectrum (Fig. 1S). The most important band attributed to the short-termed EHC_{dial} nanomaterial is depicted in the 1290-1010 cm^{-1} wavenumber range. This band indicates the presence of C–OH and ethers groups, most likely in the form of epoxides [13].

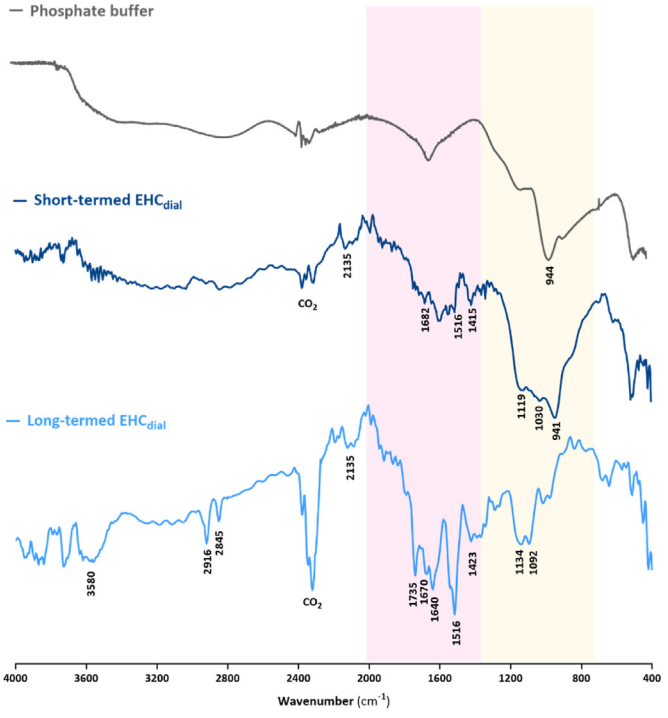

Fig. 6. ATR-FTIR spectra of short-termed EHC_{dial}, long-termed EHC_{dial}, and phosphate buffer. The shaded in yellow and pink are representative, respectively, of oxygen-containing groups in a more reduced and oxidized state.

The presence of C-OH groups is also supported by the broad band centred at 3100 cm^{-1}. Three bands emerge at 1516 cm^{-1}, 1415 (ν_s C–N) and 1682 cm^{-1} (ν_s C═O) with a low intensity. These bands point for the presence of amide groups. The assignment of the 1513 cm^{-1} peak is not straightforward since several functional groups fall in this region, like C–C str in the aromatic ring and the coupling between δ(N-H_x) and ν(C–N).

Upon 48 h of dialysis, no signal of phosphate was detected. The band assigned to C–OH groups notably decreases, while the signals in the range 1750–1512 cm^{-1} become more prominent. Within this range, the bands in 1735, 1670, and 1640 cm^{-1} are indicative of esters, carboxylic acid, and C═O groups, respectively. These results further strengthen the evidence obtained from XPS data, indicating that the dialysis process is accompanied by the further oxidation of the carbon-oxygen groups.

An interesting feature of the long-termed EHC_{dial} spectrum is the notable band at 2318 cm^{-1}, ascribed to CO_2, suggesting that this material exhibits the ability to adsorb CO_2 on its surface. Interestingly, both short-termed and long-termed dialysis show a band at 2135 cm^{-1}, assigned to a triple bond or cumulated double bonds with asymmetrical substitution (C≡C or C≡N).

Solution-state ^{1}H NMR spectroscopy provides further evidence of the structural modification promoted by dialysis. Apart from the HDO peak, no peaks appear in the spectrum of EHC_{prep}, whereas short-term EHC_{dial} reveals the presence of a doublet of doublets (dd) at δ = 3.4–3.7 ppm (typical of ABX system) and a singlet at δ = 4.5 ppm, Fig. 7 (and wide spectrum in Fig. 2S). The chemical shift of dd signal is consistent with protons of CH–O groups (alcohols or ethers), in agreement with functional groups detected by XPS and ATR-FTIR. Long-termed EHC_{dial} shows the same dd pattern but shifted to a lower field (less shielded protons). Additionally, two triplets at δ = 3.5 and 4.0 ppm are also observed, indicating that further structural modifications occur by the electrolyte removal from short-termed EHC_{dial}.

The absence of any resonance signal in the spectrum of EHC_{prep} may have two interpretations. First, it may be indicative that the edges sites are saturated with groups containing exchangeable protons, such as alcohol or carboxylic groups, in agreement with XPS and ATR-FTIR results. Another cause for the non-observation of any NMR signals comes from the presence of unpaired electrons in the EHC sample. It is well-known that the line broadening of paramagnetic species can be significant enough to cause peak merging with the baseline [18]. As it will be shown below, this sample exhibits an EPR signal, although with a low intensity.

3.3. Structural order degree

Raman spectroscopy provides comparison of the structural order degree of EHC_{prep} and EHC_{dial} (long-termed dialysis) and the detection of groups containing oxygen-oxygen bonds. Raman data recorded under 633 nm irradiation was normalized to the D band after background removal, Fig. 8. Although the spectra of EHC_{dial} and EHC_{prep} are both dominated by the typical peaks of sp^2 carbon, at 1345 cm^{-1} (band D) and 1613 cm^{-1} (band G), three other bands were also considered for a good fitting: a band centred between D and G bands at ≅ 1540 cm^{-1} associated to amorphous carbon (a-C band), a band at the right shoulder of band G related to disorder-induced features (D' band), and a band at the left side bottom of band D at ≅ 1150 cm^{-1} (D'' band). The origin of D'' band is not clear. It has been associated with the vibration of carbon atoms that are constrained by oxygen-containing groups or acetylene chains [19] or sp^3 rich phase of disordered amorphous carbon [20]. EHC_{prep} also shows a small band at 920 cm^{-1}, attributed to υ(P–O) of phosphate-electrolyte. We note that none of the EHC samples exhibit the band characteristic of H_2O_2, typically detected at 860 cm^{-1}. This result was also observed under 532 nm laser line (Fig. 3S). Comparison of the structural order degree of EHC_{prep} and EHC_{dial} is provided by I_D/I_G and $I_{a\text{-}C}/I_G$ ratio and full width of half-maximum (FWHM) of D, G, and a-C bands, Table 3. The largest FWHM of these bands, along with the highest I_D/I_G and $I_{a\text{-}C}/I_G$ ratio, was found on EHC_{dial}. These results allow to conclude that EHC_{dial} shows a lower structural degree compared to EHC_{prep}. This finding is consistent with the higher oxidation degree found in EHC_{dial}.

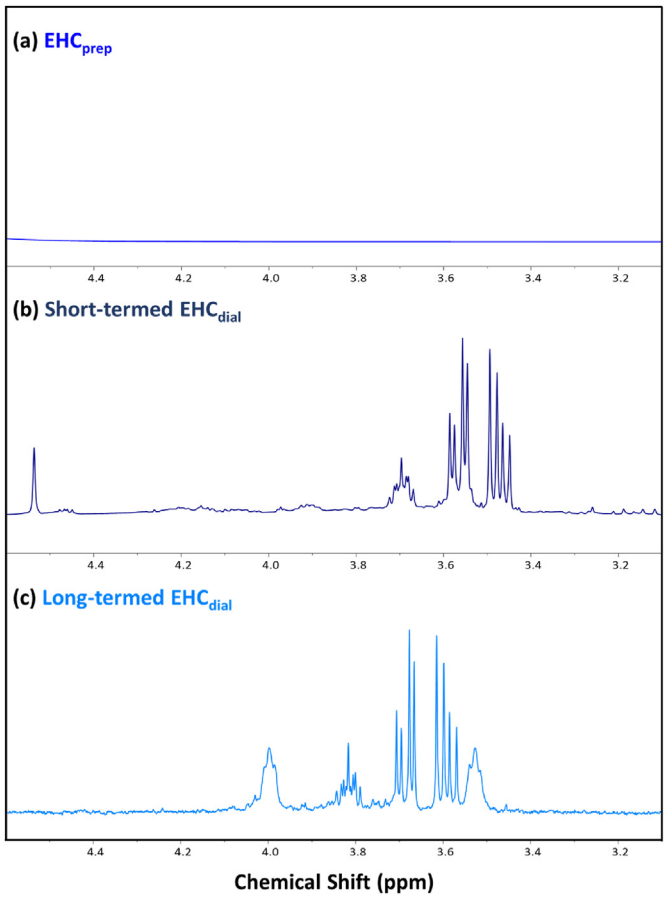

Figs. 7. ^{1}H NMR of EHC_{prep}, short-termed EHC_{dial} and long-termed EHC_{dial} solutions.

3.4. Paramagnetic properties

Unlike the aforementioned techniques, EPR was exclusively utilized for analysing the as-prepared nanomaterial solution. In this case, a more concentrated sample was used (35,2 mg C/mL). For that purpose, the galvanostatic synthesis was carried out for 2 h. To avoid interaction with gas atmosphere, the solution was manipulated under an argon stream. The nanomaterial was kept in its original aqueous medium and was frozen in liquid nitrogen before being examined by EPR at 120 K. A symmetric and sharp EPR signal with a *g* value of 2.0033 and a peak-to-trough linewidth of 4.0 G was obtained, Fig. 9. No discernible hyperfine structure was observed. The observed *g* value is typically attributed to unpaired electrons in carbon-oxygen-centred radical species [21]. However, due to the relatively weak signal, the nanomaterial fraction exhibiting paramagnetic properties must be rather small. Considering that hydroxyl groups are one of the major oxygen functional groups present on the EHC_{prep} nanomaterial, carbon-based radicals near oxygen functional groups may lead to the observed signal, as observed in graphene oxide [22].

At this point, a proposal is given to rationalize how dialysis influences the redox state of EHC. We hypothesised that the obtained results could be explained by supposing that the supporting electrolyte (phosphate buffer) enhances the stabilization of EHC_{prep} so that its removal from the EHC solution promotes an increase in the reaction rate with dissolved oxygen. The dissolved oxygen that comes into contact with the EHC material is generated *in situ* alongside the EHC nanomaterial and is also present in the ultrapure water that is used in dialysis. In the presence of

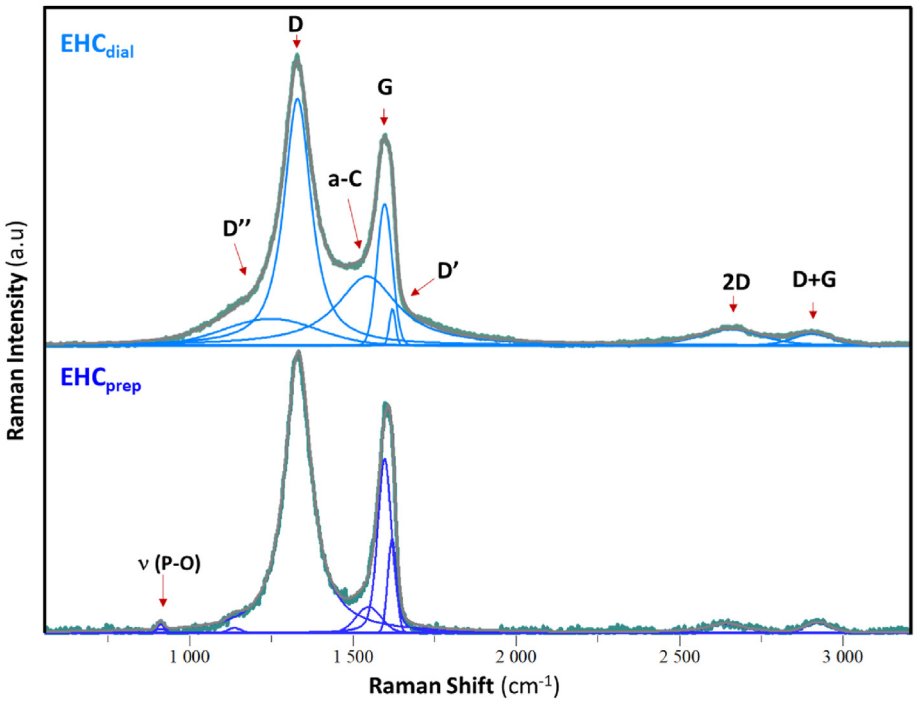

Fig. 8. Raman spectra of EHC_{prep} and EHC_{dial}, excited under 633 nm laser.

Table 3
Peaks position, intensity, and FWHM of D, G and a-C bands, as well as the I_D/I_G and $I_{a\text{-}C}/I_G$ ratio.

	D			a-C			G			I_D/I_G	$I_{a\text{-}C}/I_G$
	Position (cm $^{-1}$)	Int. (a.u)	FHWM (cm $^{-1}$)	Position (cm $^{-1}$)	Int. (a.u)	FHWM (cm $^{-1}$)	Position (cm $^{-1}$)	Int. (a.u)	FHWM (cm $^{-1}$)		
EHC_{prep}	1331.4	0.98	97.4	1546.9	0.09	90.2	1595.9	0.61	49.9	1.61	0.15
EHC_{dial}	1328.4	0.86	99.3	1541.5	0.24	224.2	1594.7	0.49	54.6	1.74	0.49

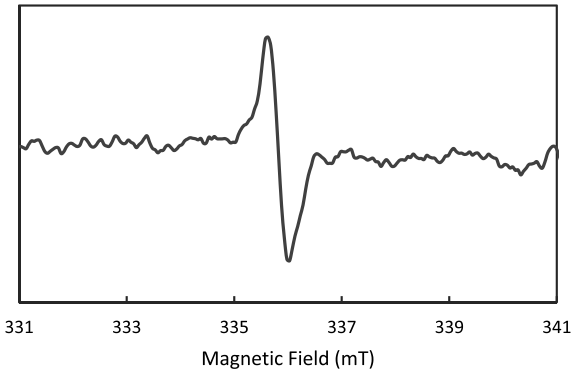

Fig. 9. EPR spectrum of as-prepared nanomaterial.

the electrolyte, EHC_{prep} may also react with O_2, but its reaction rate must be much slower. The detection of an EPR signal in EHC_{prep} is also itself consistent with the hypothesis that the electrolyte mediates the stabilization of this radical species.

Another issue, that is even more enigmatic, is the finding that EHC possesses a high affinity for Na^+ over K^+. To explain this phenomenon several requirements must be considered: a) the high ability of EHC_{dial} to adsorb on the glass material; b) the ability of adsorbed EHC_{dial} to form a supramolecular arrangement that suits the Na^+ coordinating requirements. The extensive investigation of the basic principles that govern Na^+ channel selectivity may provide clues about the factors that determine the metal coordination. In general, these are governed by the number and orientation of carboxylates and carbonyl moieties, and the number of the metal-bound water molecules [23].

4. Conclusion

Together, the results obtained from TEM, AFM, NMR, ATR-FTIR, Raman spectroscopy and XPS, reveal that the dialysis process against ultrapure water has a significant impact on various aspects of the nanomaterial's structure and properties. The removal of the electrolyte from the as-prepared nanomaterial solution affects carbon domains size, structural organization, functionalization, and crystallinity degree. After dialysis the nanomaterial is more oxidized, the carbon domains are smaller and evolve towards a linear stacking organization and an enhanced degree of amorphicity. Unexpectedly, this nanomaterial shows an anomalous high affinity for Na^+, which is exacerbated after the dialysis process (ability to capture Na^+ from the glass material in contact with the nanomaterial solution). It was also concluded that a high content of oxygen not covalently bound to carbon co-exists, either before or after the dialysis process. After dialysis, the excess oxygen is probably combined with Na^+, since a 1:1 (Na:O) stoichiometry was detected. Before dialysis, the amount of oxygen is abnormally high, suggesting that oxygen must be, in part, incorporated in the nanomaterial structure as chemisorbed O_2. In addition, it was also demonstrated qualitatively by EPR that as-prepared nanomaterial contains a small fraction with paramagnetic properties.

Briefly, this work allowed us to conclude that the structural modifications resulting from the removal of the electrolyte are a key factor to be considered during the synthesis of carbon nanomaterials, particularly when employing electrochemical approaches.

Declaration of competing interest

The authors declare no conflict of interest.

Acknowledgments

The authors thank FCT (Portugal's Foundation for Science and Technology) for financial support through the CQ-VR (UIDB/00616/2020, UIDP/00616/2020), CQE/Institute of Molecular Sciences (UIBD/00100/2020, UIPD/00100/2020 and LA/P/0056/2020), Institute for Bioengineering and Biosciences – iBB/Associate Laboratory Institute for Health and Bioeconomy - i4HB (UIDB/04565/2020, UIDP/04565/2020, and LA/P/0140/2020). ADV thanks FCT, MCTES, ESF, and EU through the individual research Ph.D. for the Ph.D. scholarship (SFRH/BD/138425/2018). RAV thanks FCT for funding through the Scientific Employment Stimulus—Institutional Call (Ref. CEECINST/00136/2021). AMF is grateful to FCT and Instituto Superior Técnico (IST), Portugal for Contract no. IST-ID/131/2018. EPR spectra were recorded at the EPSRC funded National Research Facility (EP/W014521/1).

Appendix A. Supplementary data

Supplementary data to this article can be found online at https://doi.org/10.1016/j.nanoms.2023.12.002.

References

[1] Y. Zhou, W. Zhang, R.M. Leblanc, Structure−Property−Activity relationships in carbon dots, J. Phys. Chem. B 2022 (2023) 10, https://doi.org/10.1021/acs.jpcb.2c06856.
[2] K.J. Mintz, M. Bartoli, M. Rovere, Y. Zhou, S.D. Hettiarachchi, S. Paudyal, J. Chen, J.B. Domena, P.Y. Liyanage, R. Sampson, D. Khadka, R.R. Pandey, S. Huang, C.C. Chusuei, A. Tagliaferro, R.M. Leblanc, A deep investigation into the structure of carbon dots, Carbon N Y 173 (2021) 433–447, https://doi.org/10.1016/J.CARBON.2020.11.017.
[3] A. Barreiro, F. Börrnert, S.M. Avdoshenko, B. Rellinghaus, G. Cuniberti, M.H. Rümmeli, L.M.K. Vandersypen, Understanding the catalyst-free transformation of amorphous carbon into graphene by current-induced annealing, Sci. Rep. 3 (1) (2013) 1–6, https://doi.org/10.1038/srep01115.
[4] J.J. Schneider, J.J. Schneider, Transforming amorphous into crystalline carbon: observing how graphene grows, ChemCatChem 3 (2011) 1119–1120, https://doi.org/10.1002/CCTC.201100078.
[5] S.G. Meirinho, A.M. Ferraria, A.M.B. do Rego, A.J.S. Fernandes, A.S. Viana, J.C.S. Fernandes, M.C. Oliveira, Electrochemical properties of oxygen-enriched carbon-based nanomaterials, J. Electroanal. Chem. 873 (2020) 114420, https://doi.org/10.1016/j.jelechem.2020.114420.
[6] M.C. Oliveira, A.S. Viana, A.M. Botelho do Rego, A.M. Ferraria, P.B. Tavares, A.D. Veloso, R.A. Videira, Dual behaviour of amorphous carbon released electrochemically from graphite, ChemistrySelect 1 (2016) 4126–4130, https://doi.org/10.1002/slct.201600965.
[7] A.D. Veloso, A.M. Botelho do Rego, A.M. Ferraria, L.F.V. Ferreira, D.P. Ferreira, P.B. Tavares, R. Videira, A.S. Viana, M.C. Oliveira, One-Step cathodic and anodic synthesis of hydrophilic carbon nanomaterials, Chemelectrochem 4 (2017) 2693–2702, https://doi.org/10.1002/celc.201700386.
[8] R.S.S. Vieira, A.J.S.J.S. Fernandes, M.C. Oliveira, Electrochemical behaviour of electrogenerated hydrophilic carbon nanomaterials, Electrochim. Acta 260 (2018) 338–347, https://doi.org/10.1016/j.electacta.2017.10.197.
[9] Y. Wang, W. Kong, L. Wang, J.Z. Zhang, Y. Li, X. Liu, Y. Li, Optimizing oxygen functional groups in graphene quantum dots for improved antioxidant mechanism, Phys. Chem. Chem. Phys. 21 (2019) 1336–1343, https://doi.org/10.1039/C8CP06768F.
[10] J. Deng, Q. Lu, H. Li, Y. Zhang, S. Yao, Large scale preparation of graphene quantum dots from graphite oxide in pure water via one-step electrochemical tailoring, RSC Adv. 5 (2015) 29704–29707, https://doi.org/10.1039/C4RA16805D.
[11] D. Rocco, V.G. Moldoveanu, M. Feroci, M. Bortolami, F. Vetica, Electrochemical synthesis of carbon quantum dots, Chemelectrochem 10 (2023) e202201104, https://doi.org/10.1002/CELC.202201104.
[12] W. Shi, Q. Han, J. Wu, C. Ji, Y. Zhou, S. Li, L. Gao, R.M. Leblanc, Z. Peng, Synthesis mechanisms, structural models, and photothermal therapy applications of top-down carbon dots from carbon powder, graphite, graphene, and carbon nanotubes, Int. J. Mol. Sci. 23 (2022) 1456, https://doi.org/10.3390/IJMS23031456.
[13] A.D. Veloso, M.C. Oliveira, Redox-active water-soluble carbon nanomaterials generated from graphite, J. Electroanal. Chem. 895 (2021) 115503, https://doi.org/10.1016/J.JELECHEM.2021.115503.
[14] S.G. Meirinho, A.M. Ferraria, A.M. Botelho do Rego, A.J.S. Fernandes, A.S. Viana, M.C. Oliveira, Electrogenerated hydrophilic carbon nanomaterials with tailored electrocatalytic activity, Electrochim. Acta 302 (2019) 402–413, https://doi.org/10.1016/j.electacta.2019.02.025.
[15] A.D. Veloso, A.M. Ferraria, A.M. Botelho do Rego, P.B. Tavares, P. Valentão, D.D. Pereira, P.B. Andrade, A.J. Fernandes, M.C. Oliveira, R.A. Videira, Hydrophilic carbon nanomaterials: characterisation by physical, chemical, and biological assays, ChemMedChem 14 (2019) 699–711, https://doi.org/10.1002/cmdc.201900003.
[16] A.A. Konchits, B.D. Shanina, S.V. Krasnovyd, A.I. Burya, O.Y. Kuznetsova, Paramagnetic properties of fullerene-derived nanomaterials and their polymer composites: drastic pumping out effect, Nanoscale Res. Lett. 12 (2017) 1–9, https://doi.org/10.1186/S11671-017-2241-3.
[17] P.G. Collins, K. Bradley, M. Ishigami, A. Zettl, Extreme oxygen sensitivity of electronic properties of carbon nanotubes, Science (1979) 287 (2000) 1801–1804, https://doi.org/10.1126/SCIENCE.287.5459.1801.
[18] J.D. Satterlee, Fundamental concepts of NMR in paramagnetic systems. Part II: relaxation effects, Concepts Magn. Reson. 2 (1990) 119–129, https://doi.org/10.1002/CMR.1820020302.
[19] A.C. Ferrari, J. Robertson, Origin of the 1150 cm-1 Raman mode in nanocrystalline diamond, Phys. Rev. B 63 (2001) 121405, https://doi.org/10.1103/PhysRevB.63.121405.
[20] A.Y. Lee, K. Yang, N.D. Anh, C. Park, S.M. Lee, T.G. Lee, M.S. Jeong, Raman study of D* band in graphene oxide and its correlation with reduction, Appl. Surf. Sci. 536 (2021) 147990, https://doi.org/10.1016/J.APSUSC.2020.147990.
[21] J.A. Weil, J.R. Bolton, in: Electron Paramagnetic Resonance Spectroscopy: Elementary Theory and Applications, second ed., Wiley-Interscience, 2007.
[22] B. Wang, A.J. Fielding, R.A.W. Dryfe, Electron paramagnetic resonance investigation of the structure of graphene oxide: PH-dependence of the spectroscopic response, ACS Appl. Nano Mater. 2 (2019) 19–27, https://doi.org/10.1021/acsanm.8b01329.
[23] T. Dudev, C. Lim, Factors governing the Na+ vs K+ selectivity in sodium ion channels, J. Am. Chem. Soc. 132 (2010) 2321–2332, https://doi.org/10.1021/ja909280g.